Chalcogenide Letters Vol. 22, No. 8, August 2025, p. 719 - 733

Preparation of ZnS-Carbon nanotube nanocomposites via solvothermal method and their application in electrochemical detection of escherichia coli O157:H7

F. F. Tong [a,*], J. L. Han [b]
[a] *College of Medicine & Pharmaceutical Engineering, Taizhou Vocational & Technical College, Taizhou, 318001, China*
[b] *Sino-German College, Taizhou Vocational & Technical College, Taizhou, 318001, China*

In this study, hierarchical ZnS–CNT hybrids were synthesized via a solvothermal reaction at 180 °C for 48 h, producing ~200 nm ZnS spheres uniformly anchored onto oxidized multiwalled carbon nanotubes. Structural analyses by XRD confirmed the cubic sphalerite phase, while SEM and TEM revealed a "pearl-necklace" morphology and effective nanoparticle dispersion. XPS spectra verified Zn^{2+} and oxygen-containing surface groups on the composite. Nitrogen adsorption–desorption measurements showed that incorporating CNTs transformed the material's isotherm from type III to type IV, increasing the BET surface area from 68 to 155 m^2/g and introducing mesoporosity. When drop-cast onto screen-printed electrodes and functionalized via streptavidin–biotin chemistry, the platform exhibited a concentration-dependent increase in charge-transfer resistance for E. coli O157:H7 across 10^3–10^8 CFU/mL, achieving a limit of detection of ~10^3 CFU/mL within a 30 min incubation. Specificity assays against Salmonella enteritidis, Listeria monocytogenes, and Staphylococcus aureus demonstrated negligible cross-reactivity. The rapid response, low-cost fabrication, and high surface area afforded by the mesoporous architecture highlight the composite's potential for on-site, real-time pathogen screening in food safety and environmental monitoring applications.

(Received April 27, 2025; Accepted August 14, 2025)

Keywords: Mesoporosity, Streptavidin–biotin conjugation, Charge-transfer resistance, Limit of detection, Biospecificity

1. Introduction

Nanomaterials have emerged as a cornerstone of advanced sensor technologies due to their remarkable physical and chemical properties, such as high surface-to-volume ratio, excellent electrical conductivity, catalytic activity, and enhanced chemical reactivity [1,2]. Among these materials, zinc sulfide (ZnS), a prominent II-VI semiconductor, has garnered considerable attention due to its advantageous electronic, optical, and chemical attributes [3,4]. ZnS nanoparticles, featuring a wide bandgap energy of approximately 3.7 eV [5], exhibit notable semiconductor

* Corresponding author: tztongfei123@163.com
https://doi.org/10.15251/CL.2025.228.719

characteristics and excellent stability [6], making them highly appealing for diverse applications in photocatalysis [7], optoelectronics [8], and particularly in electrochemical sensing platforms [9]. Furthermore, ZnS offers distinct benefits including cost-effectiveness, abundant availability of raw materials, and environmental friendliness compared to other heavy metal chalcogenides, rendering it a suitable candidate for scalable industrial applications [10].

Despite these intrinsic advantages, pristine ZnS nanoparticles still face limitations when employed individually in sensor applications [11,12]. Their inherent tendency towards agglomeration [13], relatively low electrical conductivity, and limited functional sites for biomolecule immobilization frequently restrict their performance [14]. These limitations can significantly impair sensor sensitivity, specificity, and stability, consequently hindering their broad-scale integration into practical sensing systems [9,15].

To address these challenges and effectively capitalize on ZnS's intrinsic properties, substantial research efforts have been directed towards the hybridization of ZnS nanoparticles with conductive carbon-based nanomaterials. Among carbon nanostructures, carbon nanotubes (CNTs) are especially favored for composite formation due to their extraordinary electrical conductivity, mechanical strength, chemical stability, and high surface area [16–18]. Incorporating CNTs into ZnS-based composites is not merely a structural enhancement but introduces synergistic interactions, substantially improving electron transfer kinetics, offering additional reactive sites, and enhancing dispersion stability in various solvent systems. The resultant ZnS@CNT composite, thus, demonstrates markedly enhanced electrochemical characteristics compared to their individual counterparts [19].

E. coli O157:H7 is recognized as one of the most dangerous foodborne pathogens, responsible for severe outbreaks characterized by hemorrhagic colitis and hemolytic uremic syndrome, occasionally leading to fatal outcomes [20,21]. Contamination by this bacterial strain is frequently associated with consumption of inadequately processed foods or water, highlighting the necessity for stringent detection methods within food safety protocols [22]. Conventionally, identification methods for E. coli O157:H7 include culture-based techniques [23], enzyme-linked immunosorbent assay (ELISA) [24], polymerase chain reaction (PCR) [25], and various chromatographic methods. While these techniques exhibit robust reliability and accuracy, significant drawbacks remain evident, particularly their prolonged detection times (typically ranging from several hours to multiple days) [26], labor-intensive procedures, and requirement for skilled personnel and sophisticated instrumentation. These drawbacks collectively limit their applicability for rapid, on-site detection and continuous monitoring.

Given these critical limitations, the development of rapid, sensitive, specific, and cost-effective electrochemical immunosensors has become a pivotal research direction [27]. Electrochemical sensors offer significant advantages in pathogen detection, including ease of operation, rapid response times, portability, and high sensitivity at relatively low costs [28]. The integration of nanocomposite materials, particularly those combining semiconductor nanoparticles with conductive carbon substrates, has significantly advanced the development of electrochemical immunosensors. The inherent electrical conductivity of CNTs coupled with the robust electrochemical activity of ZnS nanoparticles creates an ideal sensing interface, facilitating rapid electron transport and providing a suitable environment for stable immobilization of bioreceptors such as antibodies or aptamers.

Moreover, utilizing nanocomposites like ZnS@CNT enables the effective immobilization of biomolecules, enhancing both sensitivity and specificity of biosensors through improved electron transfer efficiency and greater availability of active binding sites [29,30].

The synthesis method also plays a critical role in determining the morphology, size, and surface properties of the nanocomposite [31,32], thereby directly influencing the sensor performance. Among various synthetic methodologies, solvothermal techniques offer superior control over crystal growth, morphology, and size distribution of nanomaterials under moderate temperatures and pressures [33], thus providing homogeneous distribution of ZnS nanoparticles over the CNT matrix. Consequently, the solvothermal synthesis method facilitates the generation of high-quality ZnS@CNT composites with optimized electrochemical properties essential for robust biosensor performance.

In this study, we report the preparation of ZnS@CNT nanocomposites via a carefully optimized solvothermal method, aiming to achieve enhanced electrochemical performance. Detailed material characterization was conducted to comprehensively understand the structural, morphological, and chemical attributes of the synthesized nanocomposites. Subsequently, these nanocomposites were integrated into an electrochemical immunosensor platform tailored specifically for rapid and sensitive detection of E. coli O157:H7. By leveraging the unique synergistic effects of ZnS nanoparticles and CNTs, the developed immunosensor was evaluated for sensitivity, specificity, and detection limit, highlighting its potential application in food safety and environmental monitoring.

2. Materials and methods

2.1. Materials

Zinc chloride ($ZnCl_2$), thiourea (CH_4N_2S), and multi-walled carbon nanotubes (MWCNTs, purity >95%, outer diameter 10–20 nm, length 10–30 μm) were procured from Shanghai Chemical Reagent Co., Ltd. Dimethylformamide (DMF) and ethanol were obtained from Sinopharm Chemical Reagent Co., Ltd. Streptavidin and biotin-labeled polyclonal antibodies (anti-E. coli O157:H7, concentration 5 mg/mL) were purchased from Wuhan Fine Biotech Co., Ltd. Screen-printed carbon electrodes (SPCEs, electrode area 0.2 cm^2, reference Ag/AgCl) were acquired from DropSens China. Phosphate-buffered saline (PBS, pH 7.4) and other buffer reagents were supplied by Solarbio Science & Technology Co., Ltd. Escherichia coli O157:H7 (ATCC 43888) and control bacterial strains including Salmonella enteritidis, Listeria monocytogenes, and Staphylococcus aureus were acquired from the China General Microbiological Culture Collection Center (CGMCC).

2.2. Preparation of ZnS and ZnS@CNT

ZnS nanoparticles were synthesized using a solvothermal method. Initially, 1.36 g of $ZnCl_2$ and 2.48 g thiourea were dissolved into 40 mL distilled water under vigorous stirring for 30 minutes to ensure complete dissolution. The resulting clear solution was then transferred into a Teflon-lined stainless-steel autoclave with a capacity of 50 mL. The autoclave was sealed tightly and subjected to solvothermal treatment in an electric oven at 180 °C for 48 hours. Following the completion of the reaction, the autoclave was allowed to cool naturally to room temperature. The precipitated white solid was separated by centrifugation at 10,000 rpm for 10 minutes, washed thoroughly with

ultrapure water and ethanol multiple times to remove any residual impurities, and finally dried in a vacuum oven at 60 °C overnight.

For the preparation of ZnS@CNT composites, the procedure was slightly modified by introducing multi-walled carbon nanotubes (MWCNTs). Before the reaction, MWCNTs were oxidized in concentrated nitric acid at 90 °C for 4 hours to introduce surface functionalities, facilitating homogeneous dispersion in aqueous solutions. Oxidized MWCNTs (0.02 g, 2 wt% relative to ZnS) were dispersed in the $ZnCl_2$ and thiourea precursor solution via ultrasonication for 2 hours, forming a stable suspension. The solvothermal reaction and subsequent washing and drying procedures for ZnS@CNT followed identical steps as described for pure ZnS nanoparticles.

2.3. Electrode fabrication and functionalization

Electrochemical sensing electrodes were prepared by depositing 5 μL of the ZnS@CNT dispersion (20 mg/mL in DMF) onto the active area of screen-printed carbon electrodes (SPCEs). The modified electrodes were dried at 80 °C for 20 minutes to form a uniform and stable ZnS@CNT nanocomposite layer. Subsequently, the electrodes were functionalized with streptavidin by dropping 20 μL of streptavidin solution (1 mg/mL in PBS buffer) onto the electrode surface, allowing incubation at room temperature for 2 hours. Excess streptavidin was removed by washing the electrode three times with PBS buffer. Next, 20 μL of biotin-labeled polyclonal antibodies specific for E. coli O157:H7 (100 μg/mL) were deposited onto the streptavidin-functionalized electrode and incubated overnight at 4 °C to ensure robust immobilization via biotin-streptavidin interaction. The resulting electrodes were thoroughly rinsed with PBS to eliminate unbound antibodies.

2.4. Electrochemical detection protocol

Electrochemical impedance spectroscopy (EIS) measurements were performed in a frequency range of 0.1 Hz to 100 kHz with an amplitude of 5 mV under open-circuit potential conditions in PBS buffer. To evaluate the immunosensor performance, 25 μL aliquots of bacterial suspensions at concentrations ranging from $10^1$to 10^8 CFU/mL were applied onto antibody-immobilized electrodes and incubated for 30 minutes at room temperature. Electrodes were then washed thoroughly with PBS to remove loosely attached bacteria, and electrochemical signals were recorded. PBS buffer was used as a negative control to assess nonspecific binding.

3. Results and discussion

3.1. Formation and structure characterization of ZnS and ZnS@CNT composite

The formation mechanism of ZnS and ZnS@CNT nanospheres synthesized by the solvothermal method is illustrated schematically in Figure 1. Initially, $ZnCl_2$ and thiourea dissolved uniformly in aqueous solution, generating Zn^{2+} and S^{2-} ions. Under solvothermal conditions at 180 °C, the ions interacted strongly, forming ZnS nuclei. The nuclei gradually grew and aggregated into nanoparticles driven by minimizing surface energy [34]. For pure ZnS, these nanoparticles self-assembled into uniform spherical aggregates through Ostwald ripening processes, resulting in well-defined ZnS nanospheres with smooth surfaces. In contrast, the introduction of oxidized CNTs into the reaction medium significantly influenced the nucleation and growth dynamics. CNTs, owing to

their high surface energy and abundant oxygen-containing functional groups, served as nucleation sites for ZnS nanoparticles, thus facilitating heterogeneous nucleation and growth along the nanotube surfaces. This led to the formation of a homogeneous coating of ZnS nanoparticles uniformly anchored onto the CNT surfaces, yielding the hierarchical ZnS@CNT composite structure.

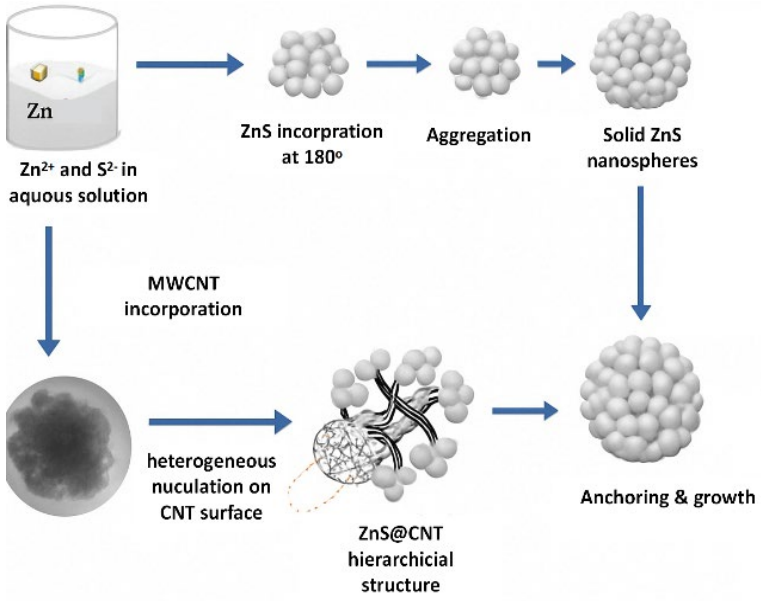

Fig. 1. Schematic illustration depicting the solvothermal synthesis pathways of pure ZnS nanospheres and ZnS@CNT composite structures.

3.2. Structural analysis

X-ray diffraction (XRD) analysis was conducted to examine the crystalline structures and phases of the synthesized ZnS and ZnS@CNT composite samples (Figure 2a). The pure ZnS sample exhibited distinct diffraction peaks at 2θ values of approximately 28.5°, 47.6°, and 56.3°, corresponding respectively to the (111), (220), and (311) planes of cubic sphalerite ZnS. These sharp, well-defined peaks indicated high crystallinity and purity of the synthesized ZnS nanoparticles [35,36]. For the ZnS@CNT composite, similar characteristic peaks were observed, confirming the retention of ZnS cubic crystal structure post-composite formation. Additionally, a broad diffraction peak at about 26.2° was detected, attributable to the (002) graphitic plane of CNTs, confirming the presence of CNTs within the composite structure [37]. The integration of CNTs slightly broadened and reduced the intensity of ZnS diffraction peaks, suggesting possible interfacial interactions between CNTs and ZnS nanoparticles and slightly reduced crystallite sizes due to the nucleation effect of CNT surfaces [38].

Scanning electron microscopy (SEM) was utilized to characterize the morphology and microstructural details of the prepared materials. Figure 2b demonstrates a typical SEM image of pure ZnS nanoparticles, clearly showing uniform, spherical aggregates with smooth surface textures [39,40]. The individual ZnS spheres exhibited an average diameter of approximately 200 nm. Upon introduction of CNTs (Figure 2c–d), a dramatic change in morphology was observed [41]. The ZnS

nanoparticles uniformly anchored onto CNT surfaces, forming continuous, interconnected hybrid structures. SEM images at lower magnification (Figure 2c) revealed excellent distribution and connectivity, while high-resolution images (Figure 2d) demonstrated a clear integration of ZnS nanoparticles along the CNT surfaces, resembling a "pearl necklace" structure [19]. This hierarchical organization significantly enhanced the surface area and electrochemical accessibility of active sites, beneficial for biosensing applications. These morphological transformations substantiate the XRD observations and underscore the successful fabrication of a ZnS@CNT composite structure with promising electrochemical properties.

Further insights into the morphology and internal structure of the ZnS and ZnS@CNT composites were obtained through Transmission Electron Microscopy (TEM). As shown in Figure 3a, the TEM image of pure ZnS nanoparticles indicated well-defined spherical structures with a relatively uniform size distribution, averaging around 200 nm in diameter. Conversely, Figure 3b reveals that the ZnS nanoparticles in the ZnS@CNT composite were evenly dispersed along the surfaces of CNTs, supporting the morphological observations from SEM analyses.

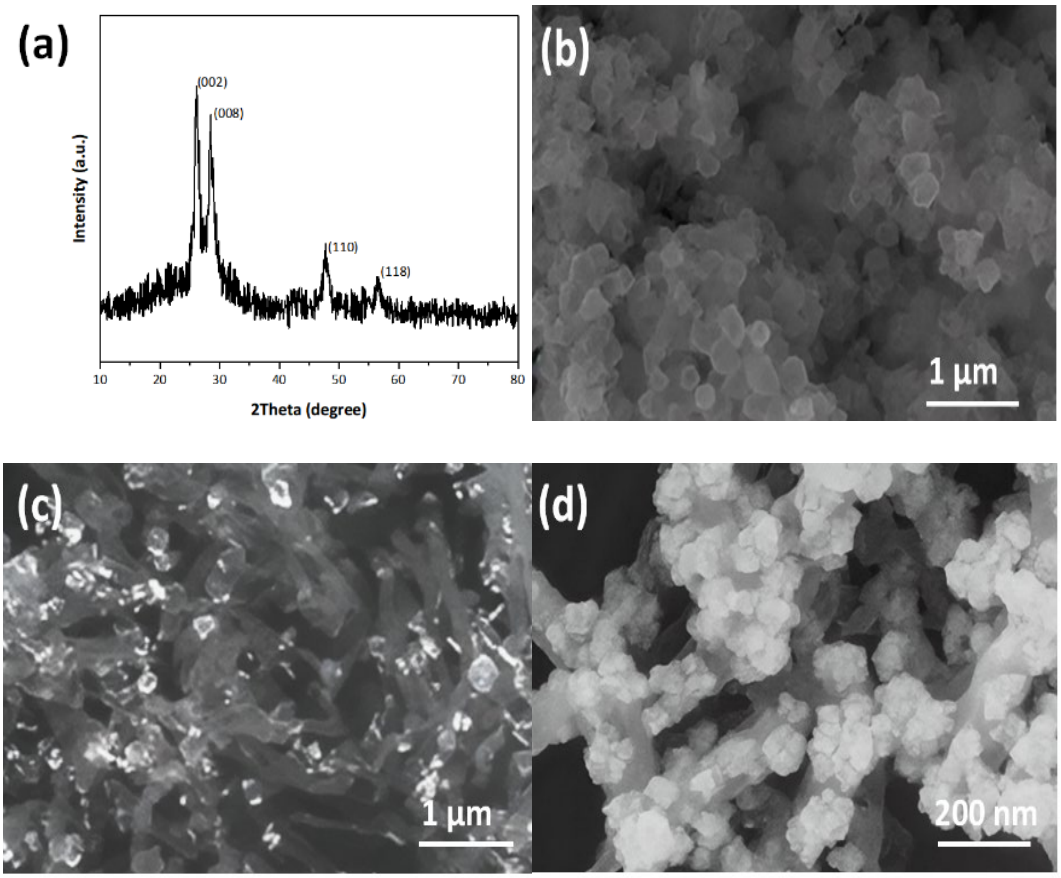

Fig. 2. (a) XRD pattern confirming the crystalline structure of the synthesized ZnS@CNT nanocomposite. (b) SEM image showing the surface morphology of pure ZnS nanospheres. (c) Low-magnification SEM image of ZnS@CNT composite revealing the overall hybrid architecture. (d) High-magnification SEM image illustrating the uniform distribution of ZnS nanoparticles on CNT frameworks.

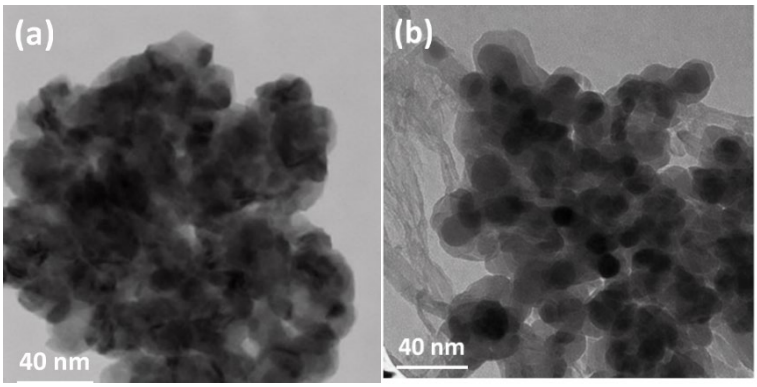

Fig. 3. TEM image of (a) ZnS and (b) ZnS@CNT.

3.3. Surface chemical composition (XPS)

The surface chemical compositions and elemental states of ZnS and ZnS@CNT composites were examined using X-ray photoelectron spectroscopy (XPS). Figure 4a presents the survey XPS spectra of both samples, clearly indicating the presence of Zn, S, and C elements [42,43]. High-resolution spectra of Zn 2p (Figure 4b) exhibited two distinct peaks at binding energies of 1022.4 eV (Zn $2p_{3/2}$) and 1045.4 eV (Zn $2p_{1/2}$), confirming the oxidation state of Zn as +2 [44,45]. Figure 4c shows the S 2p spectra, presenting doublet peaks at approximately 162.0 eV (S $2p_{3/2}$) and 163.2 eV (S $2p_{1/2}$), consistent with the sulfide state in ZnS [46]. The C 1s spectra (Figure 4d) in ZnS@CNT displayed characteristic peaks around 284.6 eV (C–C/C=C bonds), 285.8 eV (C–O bonds), and 288.6 eV (C=O bonds), indicative of functional groups introduced during CNT oxidation [47].

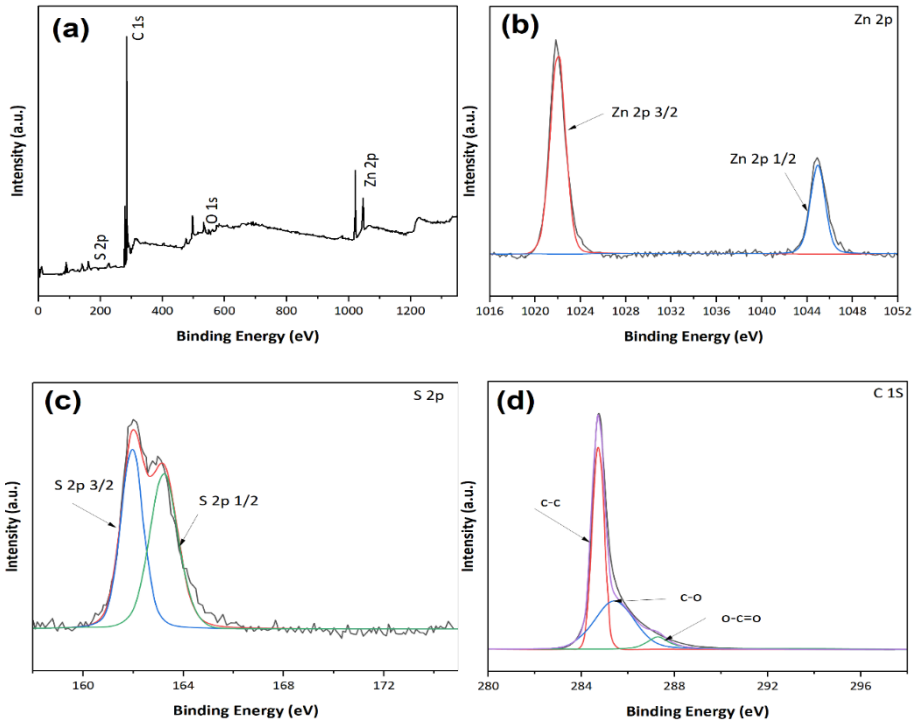

Fig. 4. (a) XPS survey spectrum of the ZnS@CNT nanocomposite, indicating elemental composition. High-resolution spectra of (b) Zn 2p illustrating the characteristic doublet of Zn^{2+}, (c) S 2p confirming the presence of sulfide species, and (d) C 1s showing contributions from CNT backbone and surface functional groups.

3.4. BET surface area analysis

BET surface area analyses of ZnS and ZnS@CNT were performed using nitrogen adsorption-desorption measurements (Figure 5). The ZnS sample exhibited a type III isotherm (Figure 5a), typical of macroporous materials, with a surface area of approximately 68 m^2/g [48]. In contrast, ZnS@CNT showed a type IV isotherm (Figure 5b) with hysteresis loops characteristic of mesoporous structures, significantly increasing the surface area to approximately 155 m^2/g. The enhanced surface area and mesoporosity of ZnS@CNT composite significantly contributed to improved electrochemical performance by providing abundant active sites for electrochemical reactions [49].

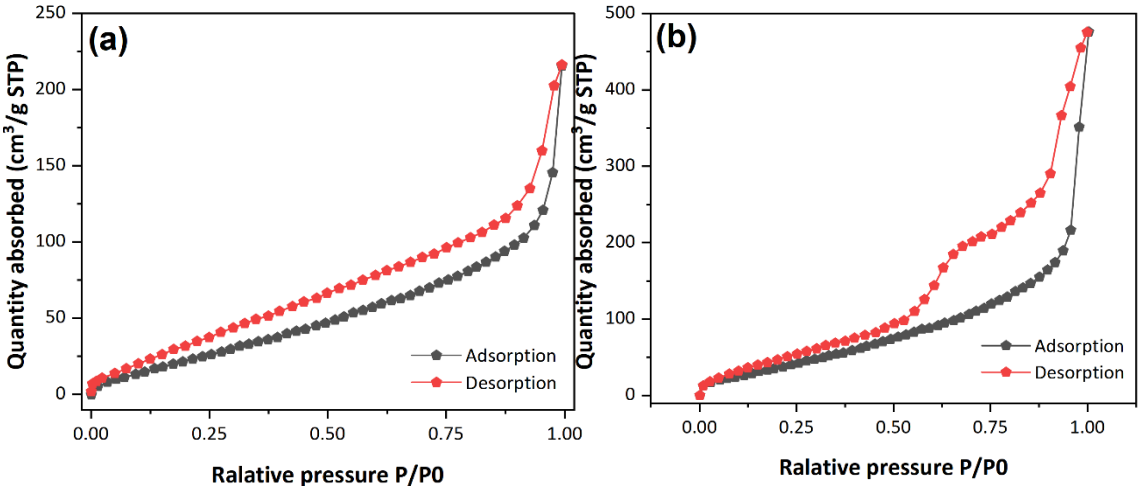

Fig. 5. Nitrogen adsorption–desorption isotherms of (a) pristine ZnS nanospheres and (b) ZnS@CNT composite, revealing distinct textural properties. The observed isotherm types and hysteresis loops reflect differences in surface area and pore structure induced by CNT incorporation.

3.5. Development of electrochemical immunosensor for E. coli detection

Figure 6 schematically illustrates the stepwise developmental process of the activated ZnS@CNT-based immunosensor designed for the rapid electrochemical detection of E. coli O157:H7. Initially, screen-printed carbon electrodes (SPCEs) were modified with ZnS@CNT composites to enhance conductivity and electrochemical surface area. Subsequently, the electrode surface was functionalized using streptavidin as a biotin-binding linker, providing a robust platform for biomolecular immobilization [50,51]. In the next step, biotin-labeled polyclonal antibodies specific for E. coli O157:H7 were immobilized via biotin-streptavidin interactions. This immobilization method ensured a strong affinity and orientation of antibodies on the electrode, facilitating the optimal antigen-antibody binding [52,53]. The immunosensor development involved careful optimization of incubation times and antibody concentrations to maximize sensitivity and reproducibility [54,55]. After antibody immobilization, unbound antibodies were removed through rigorous washing steps to minimize nonspecific signals during the detection process [56]. Finally, the sensor surface was incubated with bacterial samples for 30 minutes, after which excess or loosely bound bacteria were thoroughly washed away, leaving only specifically bound E. coli cells for electrochemical analysis.

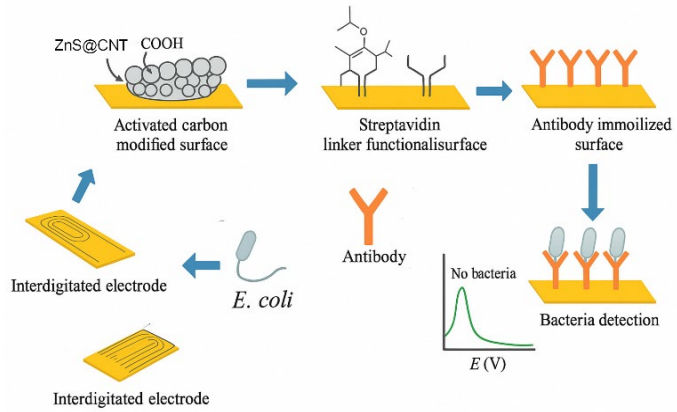

Fig. 6. Schematic representation of the sequential fabrication and functionalization steps involved in constructing the ZnS@CNT-based electrochemical immunosensor for rapid and selective detection of E. coli O157:H7.

3.6. Electrochemical performance and E. coli detection

Electrochemical impedance spectroscopy (EIS) was employed to evaluate the performance and sensitivity of the developed ZnS@CNT-based immunosensor. Figure 7a shows the resistance difference (ΔR) observed when the immunosensor was exposed to PBS buffer (control) and E. coli O157:H7 samples. The results demonstrate a significant resistance increase upon exposure to E. coli, indicative of successful bacterial binding and antibody-antigen interactions. The immunosensor exhibited a clear and reproducible response, highlighting its capability to distinguish target bacteria from control samples.

Figure 7b presents impedance amplitude spectra measured at frequencies ranging from 0.1 Hz to 100 kHz. The impedance amplitude increased noticeably after each step of sensor modification—ZnS@CNT deposition, linker attachment, antibody immobilization, and bacterial binding—indicating incremental enhancement in interfacial resistance due to successful bio-functionalization and bacterial attachment.

The phase angle spectra in Figure 7c further support these findings, showing distinct changes following each modification step. The final exposure to E. coli significantly altered the phase angle, reflecting the capacitive and resistive changes at the electrode-electrolyte interface due to bacterial cell attachment. These impedance alterations clearly illustrate the sensitivity of the immunosensor to bacterial presence. The electrochemical detection demonstrated a detection limit of approximately 10^3 CFU/mL, emphasizing the sensor's potential for rapid and sensitive detection in practical applications, such as food safety and environmental monitoring.

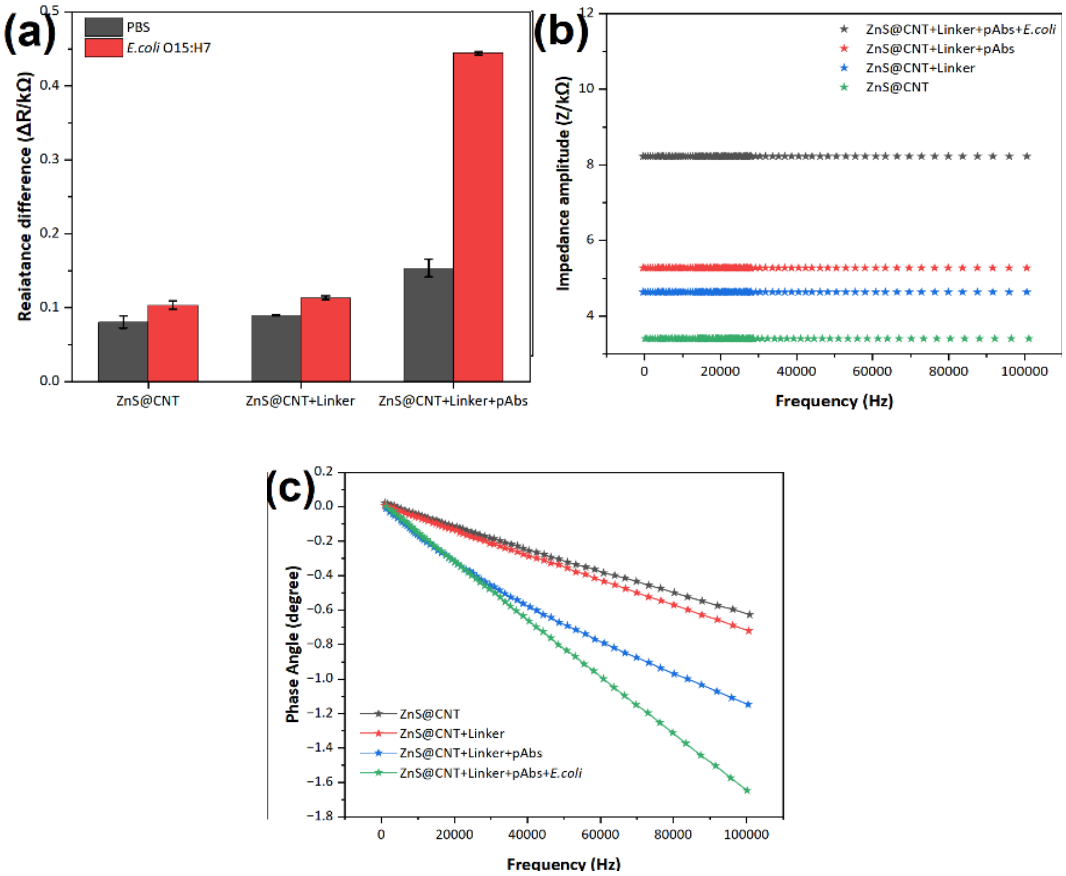

Fig. 7. (a) Change in charge transfer resistance (ΔR) of the ZnS@CNT-based immunosensor upon exposure to E. coli O157:H7, with PBS serving as the negative control. (b) Nyquist plots showing impedance amplitude variation before and after bacterial binding. (c) Corresponding phase angle spectra highlighting frequency-dependent interfacial changes induced by target recognition.

3.7. Specificity of immunosensor

The specificity of the ZnS@CNT-based immunosensor was systematically evaluated to verify its selectivity towards E. coli O157:H7 compared to other common pathogenic bacteria. Figure 8a demonstrates the dot blot assay results employing anti-E. coli polyclonal antibodies (pAbs) against various bacteria including Salmonella enteritidis, Listeria monocytogenes, Staphylococcus aureus, and the target E. coli O157:H7, alongside PBS as a negative control. The blot clearly revealed intense colorimetric spots exclusively corresponding to E. coli O157:H7, while negligible or no visible spots were observed for the other bacterial strains and the PBS control. This result explicitly highlights the high specificity of the prepared polyclonal antibodies toward E. coli O157:H7.

Further, the specificity was quantitatively assessed by using the ZnS@CNT-based immunosensor. The resistance differences (ΔR) in Figure 8b indicate significant increases exclusively for E. coli O157:H7, whereas other bacterial strains including Salmonella enteritidis, Listeria monocytogenes, Staphylococcus aureus, and PBS controls showed negligible resistance changes. The clear differentiation in ΔR values confirmed the immunosensor's robust specificity for detecting E. coli O157:H7, validating its potential for accurate pathogen detection in complex environments.

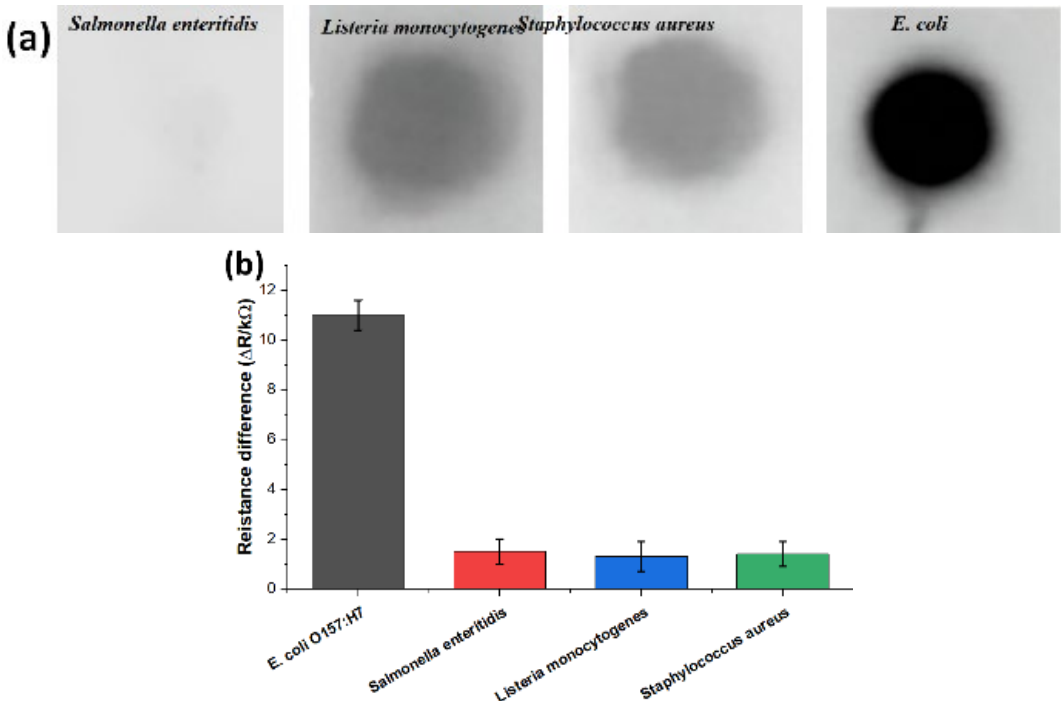

Fig. 8. Evaluation of the specificity of the custom-produced anti-E. coli O157:H7 polyclonal antibodies (pAbs) against different bacterial strains using (a) dot blot assay for qualitative antigen–antibody recognition, and (b) electrochemical response of the ZnS@CNT-based immunosensor.

3.8. LOD analysis

The detection sensitivity of the ZnS@CNT-based immunosensor was evaluated by analyzing various concentrations of E. coli O157:H7 ranging from 10^1 to 10^8 CFU/mL, as depicted in Figure 9. The resistance difference (ΔR) showed a distinct concentration-dependent response, progressively increasing with higher bacterial concentrations. Notably, the ΔR values at concentrations of 10^1 and 10^2 CFU/mL were statistically similar to that of the PBS control, indicating minimal detectable signals at these low concentrations. However, significant differences in ΔR values emerged clearly at concentrations of 10^3 CFU/mL and above, demonstrating the sensitivity threshold of the developed immunosensor. Statistical analysis revealed three distinct groups (a–c) with significant differences ($p < 0.05$) among the tested concentrations. Specifically, the detection limit of the immunosensor was determined to be approximately 10^3 CFU/mL, as this was the lowest concentration at which the sensor's response significantly deviated from the control baseline.

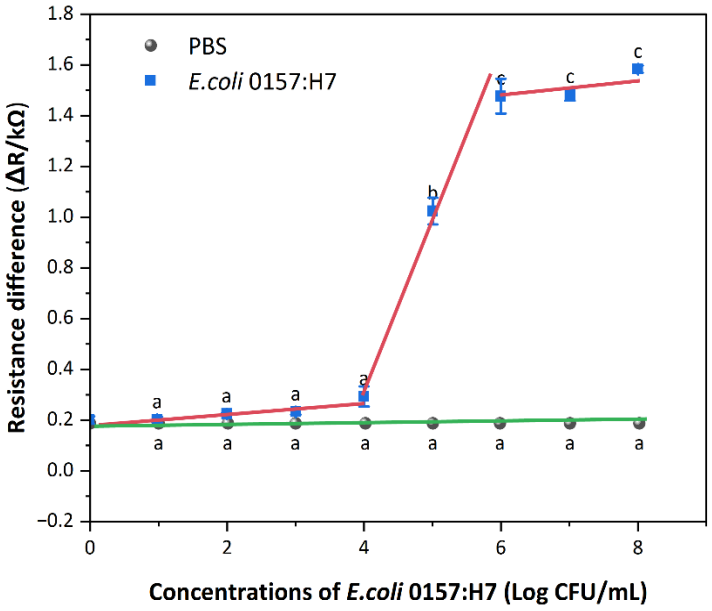

Fig. 9. Variation in charge transfer resistance (ΔR) of the ZnS@CNT-based immunosensor upon exposure to increasing concentrations of E. coli O157:H7 ranging from 10^1 to 10^8 CFU/mL.

4. Conclusion

In summary, we have demonstrated that ZnS@CNT nanocomposites synthesized via a solvothermal protocol at 180 °C for 48 h yield hierarchically structured hybrids comprising ~200 nm ZnS spheres uniformly anchored onto MWCNT frameworks, as confirmed by XRD, SEM, TEM and XPS analyses. BET measurements revealed that incorporation of CNTs transformed the textural properties from a type III isotherm with 68 m^2/g for pristine ZnS to a type IV isotherm with mesoporosity and a markedly increased surface area of 155 m^2/g, enhancing active site availability. When drop-cast onto SPCEs and functionalized through streptavidin–biotin chemistry, the ZnS@CNT-based immunosensor exhibited a dynamic detection range spanning 10^3 to 10^8 CFU/mL for E. coli O157:H7, with a limit of detection of approximately 10^3 CFU/mL following a 30 min incubation in PBS buffer. EIS and LSV measurements over a frequency window of 0.1 Hz–100 kHz showed a clear, concentration-dependent increase in charge-transfer resistance (ΔR), and phase-angle shifts corroborated efficient bacterial binding. Specificity assays against Salmonella enteritidis, Listeria monocytogenes, Staphylococcus aureus and PBS controls confirmed negligible cross-reactivity, underscoring the sensor's selectivity. The facile, low-cost fabrication and rapid 30 min response time position this immunosensor as a promising candidate for on-site food-safety monitoring. Future work will focus on miniaturization and multiplexed detection within complex matrices. Overall, the synergistic integration of semiconductor ZnS nanoparticles and conductive CNTs affords an electrochemical platform that combines high surface area, robust bioreceptor immobilization and sensitive impedance-based transduction to achieve reliable E. coli detection at clinically and industrially relevant concentrations

Acknowledgements

This work has been supported by 2024 Research Launch Fund of Taizhou Vocational & Technical College (2024GCC06); 2024 Science and Technology Plan Project of Taizhou (Design and Development of Advanced Vehicle Controller for New Energy Vehicles, Grant No. 24gyb23); 2025 Research Project on Education Science Planning of Taizhou (Grant No. TZ25106).

References

[1] S. Modi, R. Prajapati, G. Inwati, N. Deepa, V. Tirth, V. Yadav, K. Yadav, S. Islam, P. Gupta, D. Kim, B. Jeon, Crystals 12, 39 (2021); https://doi.org/10.3390/cryst12010039

[2] A. Barbosa, R. Rebelo, R. Reis, M. Bhattacharya, V. Correlo, Medical Devices & Sensors 4, (2020); https://doi.org/10.1002/mds3.10156

[3] A. Bora, A. Prudnikau, N. Fu, R. Hübner, K. Borchert, D. Schwarz, N. Gaponik, V. Lesnyak, Chemistry of Materials 34, 9251 (2022); https://doi.org/10.1021/acs.chemmater.2c02500

[4] M. Kyi, M. Aye, T. Hla, Indonesian Journal of Computer Science 13, (2024).

[5] S. Thomas, S. Kadam, Y. Ma, A. Aravind, ChemistrySelect 6, 10015 (2021); https://doi.org/10.1002/slct.202102109

[6] A. Segura, A. Rodríguez, P. Hernández, H. Pesenti, J. Hernández-Montelongo, A. Arranz, N. Benito, J. Bitencourt, L. Vergara-González, I. Ñancucheo, G. Recio-Sánchez, Nanomaterials 13, 935 (2023); https://doi.org/10.3390/nano13050935

[7] H. Naeem, H. Tofil, M. Soliman, A. Hai, S. Zaidi, N. Kizilbash, D. Alruwaili, M. Ajmal, M. Siddiq, Molecules 28, 926 (2023); https://doi.org/10.3390/molecules28030926

[8] S. Fang, J. Huang, R. Tao, Q. Wei, X. Ding, S. Yajima, Z. Chen, W. Zhu, C. Liu, Y. Li, N. Yin, L. Song, Y. Liu, G. Shi, H. Wu, Y. Gao, X. Wen, Q. Chen, Q. Shen, Y. Li, Z. Liu, Y. Li, W. Ma, Advanced Materials 35, (2023); https://doi.org/10.1002/adma.202212184

[9] D. Wang, J. Chen, Y. Li, S. Feng, Small Methods (2024).

[10] X. Song, Y. Qin, C. Yu, J. Ning, The Journal of Physical Chemistry Letters 1045 (2025); https://doi.org/10.1021/acs.jpclett.4c03405

[11] G. Debnath, P. Mukherjee, D. Waldeck, Accounts of Chemical Research (2025).

[12] L. Tang, Y. Zhang, C. Liao, L. He, X. Wu, Y. Liu, L. Sun, Nanomaterials 12, 4019 (2022); https://doi.org/10.3390/nano12224019

[13] A. Badawi, S. Alharthi, Applied Physics A 129, (2023); https://doi.org/10.1007/s00339-023-06640-y

[14] K. Olumurewa, B. Taleatu, V. Owoeye, O. Fasakin, M. Eleruja, Applied Surface Science Advances 13, 100370 (2023); https://doi.org/10.1016/j.apsadv.2023.100370

[15] R. Zeng, J. Xu, T. Liang, M. Li, and D. Tang, ACS Sensors 8, 317 (2023); https://doi.org/10.1021/acssensors.2c02314

[16] V. Naresh, J. Lee, Sensors 21, 1109 (2021); https://doi.org/10.3390/s21041109

[17] R. Dubey, D. Dutta, A. Sarkar, P. Chattopadhyay, Nanoscale Advances 3, 5722 (2021); https://doi.org/10.1039/D1NA00293G

[18] G. Speranza, Nanomaterials 11, 967 (2021); https://doi.org/10.3390/nano11040967

[19] A. Rehman, A. Afzal, M. Iqbal, M. Ali, S. Wabaidur, E. Al-Ammar, M. Imran, S. Mumtaz, E. Choi, N. Muzaffar, The Canadian Journal of Chemical Engineering 102, 226 (2023); https://doi.org/10.1002/cjce.25048

[20] B. Gelalcha, S. Brown, H. Crocker, G. Agga, O. Dego, Foodborne Pathogens and Disease 19, 598 (2022); https://doi.org/10.1089/fpd.2021.0103

[21] L. Jiang, W. Yang, X. Jiang, T. Yao, L. Wang, B. Yang, Gut Microbes 13, (2021); https://doi.org/10.1080/19490976.2021.1987783

[22] G. Zhang, Z. Huang, L. Hu, Y. Wang, S. Deng, D. Liu, J. Peng, W. Lai, ACS Nano 17, 23723 (2023); https://doi.org/10.1021/acsnano.3c07509

[23] M. Zhang, J. Liu, Z. Shen, Y. Liu, Y. Song, Y. Liang, Z. Li, L. Nie, Y. Fang, Y. Zhao, BMC Microbiology 21, (2021); https://doi.org/10.1186/s12866-021-02223-0

[24] Y. Wang, T. Bu, Y. Cao, H. Wu, X. Jia, Q. Feng, C. Xuan, L. Wang, Analytical Chemistry 95, 9237 (2023); https://doi.org/10.1021/acs.analchem.3c00743

[25] Y. Fu, Z. Ye, Y. Jia, J. Fan, M. Hashmi, C. Shen, Frontiers in Microbiology 11, (2020).

[26] A. Rani, V. Ravindran, A. Surapaneni, E. Shahsavari, N. Haleyur, N. Mantri, A. Ball, Scientific Reports 11, (2021); https://doi.org/10.1038/s41598-021-81312-6

[27] B. Mojsoska, S. Larsen, D. Olsen, J. Madsen, I. Brandslund, F. Alatraktchi, Sensors 21, 390 (2021); https://doi.org/10.3390/s21020390

[28] V. Choudhary, K. Vellengiri, L. Philip, IWA Publishing eBooks 203 (2023); https://doi.org/10.2166/9781789063714_0203

[29] V. Verma, D. Kala, S. Gupta, H. Kumar, A. Kaushal, K. Kuča, N. Martins, D. Kumar, Sensors 21, 2552 (2021); https://doi.org/10.3390/s21072552

[30] N. Abdelhamied, F. Abdelrahman, A. El-Shibiny, R. Hassan, Scientific Reports 13, (2023); https://doi.org/10.1038/s41598-023-30520-3

[31] Y. Niu, J. Liu, C. Aymonier, S. Fermani, D. Kralj, G. Falini, C. Zhou, Chemical Society Reviews 51, 7883 (2022); https://doi.org/10.1039/D1CS00519G

[32] M. Darwish, M. Mostafa, L. Al-Harbi, International Journal of Molecular Sciences 23, 1023 (2022); https://doi.org/10.3390/ijms23031023

[33] X. Kou, Y. Lin, Y. Shen, L. Tong, R. Gao, S. Liu, S. Huang, F. Zhu, G. Chen, G. Ouyang, CCS Chemistry 6, 1821 (2023); https://doi.org/10.31635/ccschem.023.202303541

[34] A. Rapakousiou, M. Minadakis, S. Chalkidis, M. Ruiz-González, C. Navío, G. Vougioukalakis, N. Tagmatarchis, ACS Applied Materials & Interfaces (2025).

[35] A. Alharthi, M. Gouda, M. Khalaf, A. Elmushyakhi, M. Taleb, H. El-Lateef, Materials 16, 777 (2023); https://doi.org/10.3390/ma16020777

[36] T. Xaba, Green Processing and Synthesis 10, 374 (2021); https://doi.org/10.1515/gps-2021-0026

[37] M. Sudhakaran, G. Veerasubramani, R. Bhattarai, G. Gnanasekaran, S. Kim, Y. Mok, ACS Applied Energy Materials 4, 2218 (2021); https://doi.org/10.1021/acsaem.0c02739

[38] Z. Zhang, F. Han, J. Fang, C. Zhao, S. Li, Y. Wu, Y. Zhang, S. You, B. Wu, W. Li, CCS Chemistry 4, 880 (2021); https://doi.org/10.31635/ccschem.021.202100825

[39] A. Kumar, S. Mukherjee, H. Sharma, U. Dwivedi, S. Kumar, R. Gangwar, R. Choubey, Physica Scripta 97, 045819 (2022); https://doi.org/10.1088/1402-4896/ac6078

[40] A. AL-Zahra, A. Al-Sammarraie, Chemical Methodologies 6, 67 (2022).

[41] X. Liu, X. Wei, Z. Zhang, X. Wang, G. Liu, D. Luo, J. Li, Renewables 1 (2024).

[42] H. Peng, J. Xiao, Z. Wu, L. Zhang, Y. Geng, W. Xin, J. Li, Z. Yan, K. Zhang, Z. Zhu, CCS Chemistry 5, 1789 (2022); https://doi.org/10.31635/ccschem.022.202202276

[43] Z. Wang, L. Chen, D. Wang, Z. Ding, X. Zhang, X. Feng, L. Jiang, CCS Chemistry 4, 1044 (2021); https://doi.org/10.31635/ccschem.021.202100842

[44] N. Li, D. Si, Q. Wu, Q. Wu, Y. Huang, R. Cao, CCS Chemistry 5, 1130 (2022); https://doi.org/10.31635/ccschem.022.202201943

[45] X. Zeng, S. Zhang, T. Long, Q. Zhao, H. Wang, W. Ling, X. Wu, A. Yu, Z. Chen, Renewables 2, 52 (2024); https://doi.org/10.31635/renewables.024.202300045

[46] H. Lv, L. Sun, D. Xu, W. Li, B. Huang, B. Liu, CCS Chemistry 4, 2854 (2021); https://doi.org/10.31635/ccschem.021.202101343

[47] K. Jiang, X. Ma, S. Back, J. Zhao, F. Jiang, X. Qin, J. Zhang, W. Cai, CCS Chemistry 3, 241 (2020); https://doi.org/10.31635/ccschem.020.202000667

[48] B. Raffah, H. Hassan, M. Iqbal, Y. Al-Hadeethi, Energy & Fuels 38, 3477 (2024); https://doi.org/10.1021/acs.energyfuels.3c04598

[49] E. Sharifpour, P. Arabkhani, F. Sadegh, A. Mousavizadeh, A. Asfaram, Scientific Reports 12, (2022); https://doi.org/10.1038/s41598-022-16676-4

[50] F. Oberhaus, D. Frense, D. Beckmann, Biosensors 10, 45 (2020); https://doi.org/10.3390/bios10050045

[51] A. Sobhan, F. Jia, L. Kelso, S. Biswas, K. Muthukumarappan, C. Cao, L. Wei, Y. Li, Biosensors 12, 908 (2022); https://doi.org/10.3390/bios12100908

[52] A. Domínguez-Aragón, E. Zaragoza-Contreras, G. Figueroa-Miranda, A. Offenhäusser, D. Mayer, Biosensors 13, 63 (2022); https://doi.org/10.3390/bios13010063

[53] H. Kim, D. Park, Y. Park, D. Kim, J. Kim, Nano Letters 22, 6537 (2022); https://doi.org/10.1021/acs.nanolett.2c01584

[54] J. Lou, X. Chu, X. Yang, Y. Zou, Z. Hong, O. Huang, Alexandria Engineering Journal 88, 182 (2024); https://doi.org/10.1016/j.aej.2024.01.036

[55] J. Plooy, B. Kock, N. Jahed, E. Iwuoha, K. Pokpas, Molecules 28, 8022 (2023); https://doi.org/10.3390/molecules28248022

[56] S. Fakhraldeen, S. Berry, D. Beebe, A. Roopra, C. Bisbach, V. Spiegelman, N. Niemi, C. Alexander, Journal of Biological Chemistry 298, 101649 (2022); https://doi.org/10.1016/j.jbc.2022.101649